Paleoceanography and Paleoclimatology

RESEARCH ARTICLE
10.1029/2020PA003853

Special Section:
The Miocene: The Future of the Past

Middle Miocene Intensification of South Asian Monsoonal Rainfall

Xueping Yang[1], Jeroen Groeneveld[2], Zhimin Jian[3], Stephan Steinke[1], and Liviu Giosan[4]

[1]Department of Geological Oceanography and State Key Laboratory of Marine Environmental Science, Xiamen University, Xiamen, China, [2]Alfred Wegener Institute, Helmholtz Center for Polar and Marine Research, Potsdam, Germany, [3]State Key Laboratory of Marine Geology, Tongji University, Shanghai, China, [4]Geology and Geophysics, Woods Hole Oceanographic Institution, Woods Hole, MA, USA

Key Points:
- We present the first South Asian monsoon (SAM) rainfall record for the Eastern Arabian Sea region for the middle to late Miocene
- We find an intensification of SAM rainfall from ~15 to 11 Ma
- Intensification of the SAM is consistent with climate models of an overall strengthening Asian monsoon from the Eocene to late Miocene

Correspondence to:
S. Steinke,
ssteinke@xmu.edu.cn

Citation:
Yang, X., Groeneveld, J., Jian, Z., Steinke, S., & Giosan, L. (2020). Middle Miocene intensification of South Asian monsoonal rainfall. *Paleoceanography and Paleoclimatology*, *35*, e2020PA003853. https://doi.org/10.1029/2020PA003853

Received 17 DEC 2019
Accepted 25 NOV 2020
Accepted article online 27 NOV 2020

Abstract During the middle Miocene, Earth's climate changed from a global warm period (Miocene Climatic Optimum) into a colder one with the expansion of the Antarctic ice sheet. This prominent climate transition was also a period of drastic changes in global atmospheric circulation. The development of the South Asian monsoon is not well understood and mainly derived from proxy records of wind strength. Data for middle Miocene changes in rainfall are virtually non-existent for India and the Arabian Sea prior to 11 Ma. This study presents planktic foraminiferal trace element (Mg/Ca and Ba/Ca) and stable oxygen isotope records from NGHP-01 Site 01A off the coast of West India in the Eastern Arabian Sea (EAS) to reconstruct the regional surface hydrography and hydroclimate in the South Asian monsoon (SAM) region during the middle Miocene. The Ba/Ca and local seawater $\delta^{18}O$ ($\delta^{18}Osw$) changes reveal a notable gradual increase in SAM rainfall intensity during the middle Miocene. Additionally to this long-term increase in precipitation, the seawater $\delta^{18}O$ is punctuated by a prominent decrease, i.e. freshening, at ~14 Ma contemporary with Antarctic glaciation. This suggests that Southern Ocean Intermediate Waters (SOIW) transmitted Antarctic salinity changes into the Arabian Sea via an "oceanic tunnel" mechanism. The middle Miocene increase in SAM rainfall is consistent with climate model simulations of an overall strengthening Asian monsoon from the Eocene to the middle/late Miocene with a further acceleration after the middle Miocene climate transition.

1. Introduction

The South Asian monsoon (SAM) is a complex coupled atmosphere-ocean-land phenomenon, marked by seasonal reversals in wind direction accompanied by changes in seasonal rainfall and an important conveyor of interhemispheric exchange of moisture and energy (e.g., An et al., 2011). However, the geological history and evolution of the SAM are not well understood and unresolved issues still exist. In particular, the evolution and timing of the onset and intensification of the SAM winds and rainfall to modern strength are still disputed (e.g., Gupta et al., 2015). It is of crucial importance to determine the exact timing of when and how the SAM appeared and evolved over time as well as the character of changes in order to understand the mechanism and controlling factors that drove the SAM system. Most of the evidence for the long-term history and evolution of the SAM is derived from records of wind strength and the associated upwelling in the Arabian Sea (Gupta et al., 2015; Nigrini, 1991; Zhuang et al., 2017) and deposits of wind-driven currents from the Maldives (Betzler et al., 2016). Based on the first appearance of siliceous biota, Nigrini (1991) suggested an age of 11.9 Ma for the onset of upwelling in the western Arabian Sea (WAS). Isotopic and faunal records from the Oman margin and Owen Ridge in the WAS suggest that modern summer monsoonal wind patterns were established after 12.9 Ma (Gupta et al., 2015). Betzler et al. (2016) confirmed this age for the apparent onset of the modern SAM wind system. Sea surface temperature (SST) records from the WAS indicate the establishment of monsoonal summer upwelling between 11 and 10 Ma (Zhuang et al., 2017). However, planktic foraminiferal records from the WAS show the first appearance of planktic foraminifera *Globigerina bulloides*, a proxy indicator for upwelling intensity and thus monsoonal wind strength, at ~14.5 Ma (Kroon et al., 1991). Evidence for an earlier onset of the modern monsoonal wind patterns also comes from the recent study of Bialik et al. (2020), which suggests that the western Indian Ocean upwelling and oxygen minimum zone (OMZ) were most likely established between ~14.8 and 14.0 Ma. Whether the proposed onset of the SAM winds between ~14.8 and 10 Ma is associated with changes in rainfall,

a defining characteristic of monsoon systems is not known because rainfall reconstructions are virtually non-existent for the Peninsular India and the Arabian Sea region for the period ~14.8 to 10 Ma. Stable isotope profiles of fossil freshwater bivalve shells and mammal teeth from the Himalayan foreland basin indicate strong seasonality in precipitation since at least 11 Ma (Dettman et al., 2001). Further evidence for a relatively humid climate in the SAM region between 15 and 10 Ma comes from palaeo-botanical proxy records (Hoorn et al., 2000; Prasad, 1993; Srivastava et al., 2018). In contrast, hydrogen isotopic ratios of leaf wax at Ocean Drilling Program (ODP) Site 722 (WAS) indicate that the source regions (Pakistan, Iran, Afghanistan, and the Arabian Peninsula) for the plant waxes became progressively drier from 10 to 5.5 Ma (Huang et al., 2007). Climate modeling studies suggest that the SAM has been operating at least since the late Eocene (e.g., Huber & Goldner, 2012; Licht et al., 2014) and that an active and intense SAM existed during the early/middle Miocene (Herold et al., 2011). Early/middle Miocene pollen assemblages from the siliciclastic Ambalapuzha Formation at the coastal cliffs of Varkala in southwest Kerala, India, reveal a modern-like annual temperature and precipitation cycle with only minor reduction in rainfall seasonality during the Miocene Climatic Optimum (MCO, ~17–15 Ma; Reuter et al., 2013), indicating an active SAM during the early/middle Miocene.

We present an ~5 Myr (16–11 Ma) record of changes in SAM rainfall recorded at site NGHP-01-01A from the Eastern Arabian Sea (EAS) off the coast of western India (Figure 1). Site NGHP-01-01A is considered ideal to provide a very sensitive record for changes in SAM precipitation. The core location has freshwater delivered either directly as rainfall, or via runoff from the Western Ghats during the summer SW monsoon season (Figure 1). This is because the west coast of India and the adjacent EAS receive highest rainfall during the summer SW monsoon season (June to September; Figure 1b). While the majority of rivers of Peninsular India mainly emerging from the Western Ghats flow eastward into the Bay of Bengal (BoB), the Narmada, and the Tapti are the only major rivers that flow into the Arabian Sea (Figure 1e). Several smaller rivers (e.g., Kalinadi, Gangavati, Sharavati, Periyar, Valapattam, Bharathpuzha, Pamba, and Netravati) also originate in the Western Ghats and flow westward, draining into the Arabian Sea and thus represent a major freshwater source for the coastal EAS (Figure 1e; Milliman & Farnsworth, 2011). High rainfall on the west coast of India and river runoff from the Western Ghats result in an increased freshwater flux and the development of low-salinity surface waters off the western coast of India during the summer SW monsoon season, affecting our core location (Figure 1; e.g., Sarkar et al., 2000). Since the formation of the Western Ghats at ~50 Ma (Gunnell et al., 2003), the Western Ghats have insured that orographically controlled rainfall is a constant in the hydroclimate of the EAS region. During the winter, the EAS area is under minor influence by the intrusion of low-salinity water from the BoB, which is related to summer runoff into the BoB. Low-salinity BoB water is carried by the southward flowing East Indian Coastal Current (EICC) and then fed into the West India Coastal Current (WICC), which flows northward into the EAS (e.g., Prasanna Kumar et al., 2004; Figure 1c). A recent numerical modeling study by Behara et al. (2019) has suggested that the freshening of the EAS during the winter is related to rainfall during the early winter in the southwestern BoB between 6°N and 15°N. However, this view is challenged by observations from surface drifters and Argo floats, which reveal that the WICC does not continuously carry surface freshwater from the BoB to the EAS during the winter monsoon (Hormann et al., 2019). Conversely, during the summer monsoon season, the equatorward-moving WICC, which strengthens southward, advects slightly higher salinity water toward the south along the west coast of India (Prasanna Kumar et al., 2004; Figure 1d). The seasonal changes in rainfall and surface water circulation in the EAS as described above are reflected in the hydrography at our Site NGHP-01-01A (Figures 1c and 1d). Site NGHP-01-01A experiences low-salinity conditions from January to June (~35.7 psu) due to the minor intrusion of low-salinity water from the BoB which is related to summer monsoonal runoff and reaches the core site in winter and to runoff from the Western Ghats during June when summer monsoonal rainfall is highest at the west coast of India. Salinity is higher (~36.3 psu) from July to December. This is related to decreasing summer monsoonal rainfall and the influence of equatorward-flowing WICC which carries slightly higher salinity waters from the northern Arabian Sea toward the south (Prasanna Kumar et al., 2004).

Here, we reconstruct relative sea surface water salinities based on combined measurements of Mg/Ca ratios and stable oxygen isotopes in tests of the planktic foraminifera *Trilobatus sacculifer-quadrilobatus* to constrain local seawater $\delta^{18}O$ ($\delta^{18}O_{sw}$ = proxy for sea surface salinity; e.g., Nürnberg, 2000) in order to reconstruct the hydrography of the EAS surface waters and thus changes in rainfall of the SAM region.

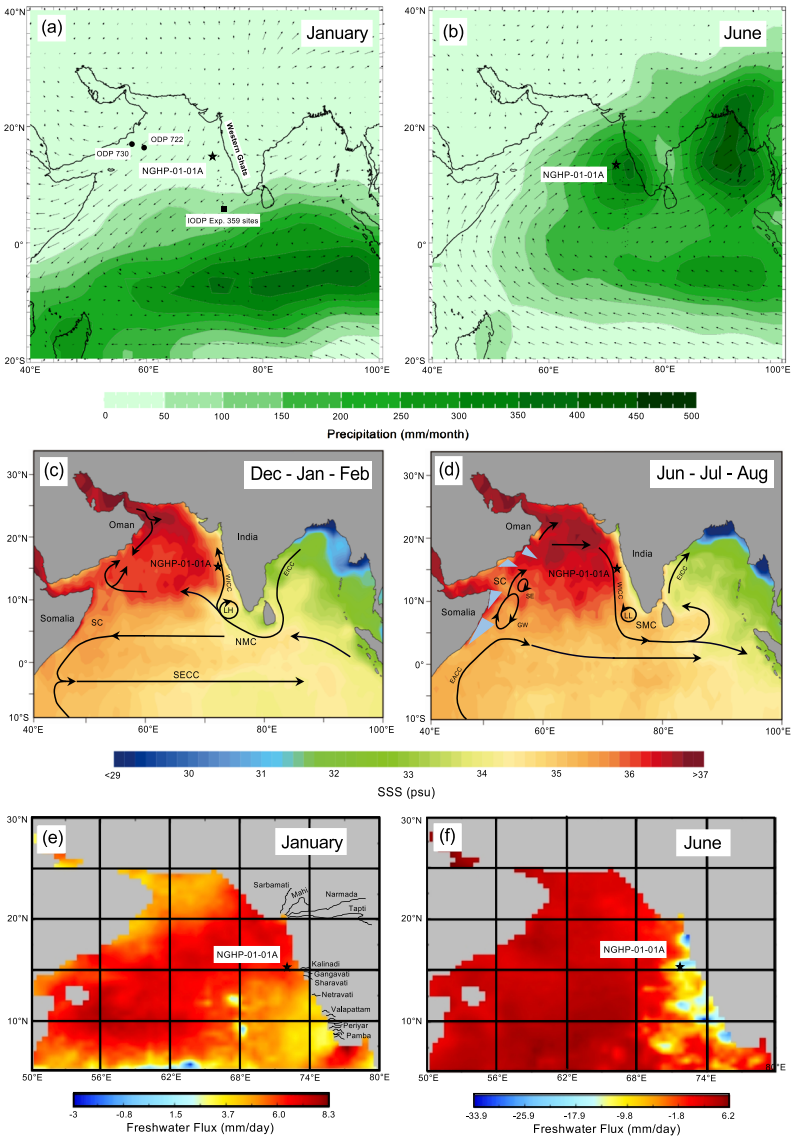

Figure 1. (a and b) Map of precipitation, surface wind direction, and strength over the northern Indian Ocean for (a) January (winter NE monsoon) and (b) June (summer SW monsoon). Map (a) also shows the position of marine sediment core NGHP-01-01A (2006 Indian National Gas Hydrate Program Expedition-01). The locations of other cores discussed in the text are also indicated: IODP Expedition sites (Sites U1466, U1468, and U1471), Betzler et al. (2016); ODP Site 730, Gupta et al. (2015) and Zhuang et al. (2017); ODP Site 722 (Kroon et al., 1991), Zhuang et al. (2017), and Bialik et al. (2020). Monthly precipitation and surface wind speed and strength for the 925 hPa pressure level (arrows with speed proportional to the vectors) is derived from National Centers for Environmental Prediction (NCEP) reanalysis (http://iridl.ledeo.columbia.edu). Note the high rainfall on the southwestern margin of India during the summer SW South Asian monsoon season in the vicinity of Site NGHP-01-01A. (c and d) Salinity and schematic representation of the surface ocean circulation (black lines) in the northern Indian Ocean in (c) December-January-February (winter NE monsoon) and (d) June-July-August (summer SW monsoon); SMC, Southwest Monsoon Current; NMC, Northwest Monsoon Current; WICC, West India Coastal Current; EICC, East India Coastal Current; SC, Somali Current; SECC, South Equatorial Countercurrent; EACC, East African Current; LH, Laccadive High, LL, Laccadive Low; GW, Great Whirl; SE, Socotra Eddy. Upwelling wedges are indicated in light blue (as inferred from Schott & McCreary, 2001). The salinity data are from the JPL (Jet Propulsion Laboratory) SMAP-SSS V4.2 CAP (daily 8 day running mean, level 3; Fore et al., 2016; https://doi.org/10.5067/SMP42-3TPCS) product from NASA's (National Aeronautics and Space Administration) SMAP (Soil Moisture Active Passive) observator. (e and f) Monthly average freshwater flux (Evaporation-Precipitation; Fennig et al., 2012) during the winter SAM (January) (e) and during the summer SAM (June) (f). Rivers which originate in the Western Ghats and flow westward, draining into the Arabian Sea are given in (e). Note the high freshwater flux on the southwestern margin of India during the summer SAM in the vicinity of Site NGHP-01-01A (f).

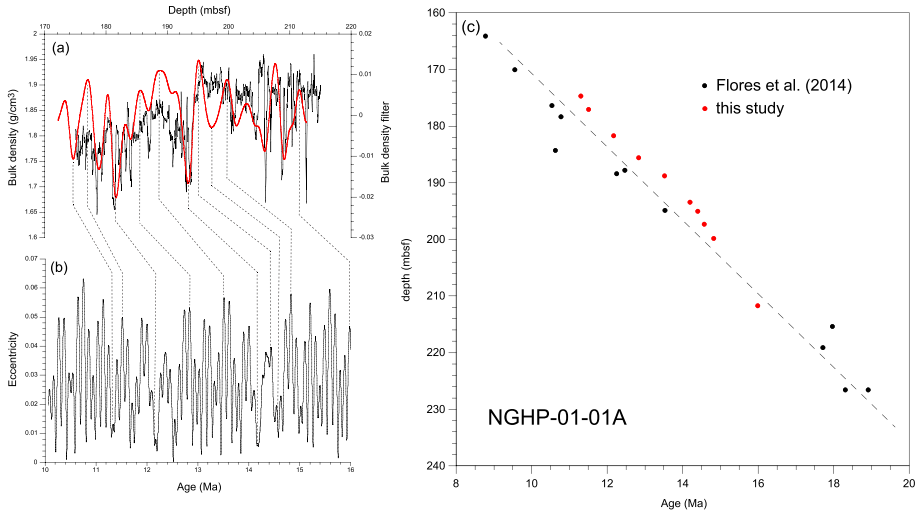

Figure 2. (a) Bulk density measurements of Site NGHP-01-01A (Collett et al., 2007). A spectral analysis of the bulk density data in the depth interval was performed followed by filtering the signal of the dominant cycle (1 cycle per ~4 m). Considering the number of cycles present in this filter and the shipboard biostratigraphy, this cycle is identified as the 405 kyr eccentricity, which is the dominant cyclicity in middle Miocene climate records (De Vleeschouwer et al., 2017; Holbourn et al., 2007). In a next step the 405 kyr filter was correlated to the orbital solution of eccentricity (b) (Laskar et al., 2004) to acquire the tie-points for constructing the age model for this study. (c) Distribution of calcareous nannofossil and planktonic foraminifera events versus age according to ATNTS04 (Astronomical Tuned Neogene Time Scale; Gradstein et al., 2004) scale of Site NGHP-01-01A (black dots; Flores et al., 2014) and age control points used to construct the age model for Site NGHP-01-01A in the depth interval 212–172 mbsf (~16–11 Ma; red dots).

In addition, we analyzed planktic foraminiferal Ba/Ca ratios of the same samples. Similar to the salinity reconstructions, Ba/Ca ratios in planktic foraminifera shells also serve as a proxy for relative salinity, albeit purely related to river/continental runoff (Bahr et al., 2013; Groeneveld et al., 2018; Hönisch et al., 2011; Lea & Boyle, 1991) and thus can provide important information about changes of continental monsoonal rainfall.

2. Materials and Methods

2.1. Site Description and Age Model

The analyzed material was sampled from Site NGHP-01-01A (2006 Indian National Gas Hydrate Program Expedition-01, 15°18.366′N, 70°54.192′E, water depth 2,663 m, Collett et al., 2007). Site NGHP-01-01A was drilled by the drill ship JOIDES Resolution (JR) in the Kerala-Konkan Basin and recovered foraminifera-bearing nannofossil oozes (Figure 1; Collett et al., 2007). The terrigenous portion of the sediment accumulated at Site NGHP-01-01A primarily originates from the adjacent Western Ghats range (Campanile et al., 2008). The initial age model of Site NGHP-01-01A was based on a combination of calcareous nannofossil and planktic foraminiferal biostratigraphic events (Flores et al., 2014). The biostratigraphic age constraints suggest that Site NGHP-01-01A represents an uninterrupted record from the early Oligocene to the Holocene with no hiatuses (Flores et al., 2014). To constrain the age model for the time interval in this study, we used orbital tuning of the bulk density measurements acquired via wireline logging at a resolution of 2.5 cm (Collett et al., 2007) for the depth interval 212–172 mbsf (Figure 2). Using the Analyseries software (Paillard et al., 1996), spectral analysis of the density data in the depth domain was performed followed by filtering the signal of the dominant cycle (1 cycle per ~4 m). Considering the number of cycles present in this filter and the shipboard biostratigraphy, this cycle is identified as the 405 kyr eccentricity, which is the dominant cyclicity in middle Miocene climate records (De Vleeschouwer et al., 2017; Holbourn et al., 2007). In a next step the 405 kyr filter was correlated to the orbital solution of eccentricity (Laskar et al., 2004) to acquire the tie-points for constructing the age model for this study (Table 1; Figure 2). Comparison with the shipboard biostratigraphy supports the validity of this approach (Figure 2). Sedimentation rates (m/Myr) in the depth interval 212–172 mbsf (~16–11 Ma) range between 4.6 and 11.3 m/Myr.

Table 1
Age Control Points Used to Construct the Age Model and Linear Sedimentation Rates (m/Ma) for Site NGHP-01-01A in the Depth Interval 212–172 mbsf (~16–11 Ma)

Depth (mbsf)	Age (Ma)	LSR (m/Ma)
174.67	11.303	11.28
177.05	11.514	7.15
181.75	12.171	5.83
185.65	12.840	4.63
188.81	13.522	6.93
193.45	14.192	7.81
195.09	14.402	12.87
197.33	14.576	10.16
199.85	14.824	10.20
211.73	15.989	

2.2. Foraminiferal Isotopic and Elemental Analysis

A total of 122 samples was processed for planktic foraminiferal stable oxygen isotope and 117 samples for trace element/Ca analyses with an average time resolution of ~40 kyr between 172 and 210 m below seafloor (mbsf). In addition, 174 samples from the same depth interval were processed for benthic foraminiferal stable oxygen isotope analyses in order to further constrain our age model. Stable isotope analyses were determined on samples composed of around ~5–15 *T. sacculifer-quadrilobatus* specimens of the 250–355 μm size fraction. Only specimens without sac-like final chambers have been used for isotope and trace element analyses. The isotopic composition of all planktic foraminifera samples was measured at MARUM, University of Bremen, Germany, using a Finnigan MAT 251 mass spectrometer, connected with an automatic line for carbonate preparation (type "Kiel III"). Analytical standard deviation is about ±0.07%. Two to five specimens of benthic foraminifera *Planulina wuellerstorfi* (also commonly referred to as *Cibicidoides*, *Cibicides*, or *Fontbotia*) and *Cibicidoides mundulus* which is regarded to be a junior synonym to *Cibicidoides kullenbergi* (Holbourn & Henderson, 2002; Holbourn et al., 2013) were picked from the >150 μm size fraction. The stable isotope composition was measured by a Finnigan-MAT253 mass spectrometer equipped with an automatic carbonate preparation device (Kiel III) at the State Key Laboratory of Marine Geology, Tongji University. The standard deviation is ±0.07‰ for $\delta^{18}O$. Combining these species is justified by the fact that paired measurements of *C. wuellerstorfi* and *C. kullenbergi* revealed that there is no offset between the $\delta^{18}O$ values of the two species (e.g., Martinez-Mendez et al., 2013). The benthic foraminiferal $\delta^{18}O$ values are presented in "*Uvigerina*-scale" by adding 0.64‰ (Shackleton & Opdyke, 1973).

Elemental analyses were performed on approximately 30 tests per sample of *T. sacculifer-quadrilobatus* of the 250–355 μm size fraction. Foraminiferal tests were cleaned in successive steps following the cleaning protocol by Barker et al. (2003). This is composed of ultra-sonication and rinses with ultrapure water and methanol to remove clays, oxidation for removal of organic matter and a final acid leach to remove any adsorbed contaminants. After the cleaning, all samples were inspected under a microscope and any particles that were still present in the sample, such as black and brown bits and micro-nodules that are likely Mn-Fe-oxyhydroxides, were manually removed. The elemental concentrations were analyzed on an ICP-MS (Thermo X7) at the State Key Laboratory of Marine Geology, Tongji University Shanghai, China, following the elemental determination method developed by Yu et al. (2005). Mass drift, matrix effects, and long-term instrumental precision were monitored by replicates of an in-house standard (Mg/Ca = 3.02 mmol/mol; Ba/Ca = 1.62 μmol/mol). The relative standard deviations for the in-house standard were 0.02 mmol/mol (0.89%) for Mg/Ca and 0.02 μmol/mol (1.32%) for Ba/Ca. Replicate measurements (re-picked and separately cleaned) of *T. sacculifer-quadrilobatus* samples (n = 25) revealed an average standard deviation of 0.10 mmol/mol for Mg/Ca and 0.33 μmol/mol for Ba/Ca, respectively. Al/Ca and Mn/Ca ratios were determined in conjunction with Mg/Ca to assess the effectiveness of the cleaning procedure to remove clay minerals and the occurrence of syn-sedimentary and post-depositional Mn-oxyhydroxides and/or Mn-rich carbonate coatings, respectively.

Mixed layer temperature (°C) estimates were obtained by using the species-specific equation for *T. sacculifer* (Anand et al., 2003; Mg/Ca [mmol/mol] = 0.347 exp [0.090 × T, °C]). The errors of the temperature reconstructions are estimated by propagating the errors introduced by the Mg/Ca measurements and the Mg/Ca-temperature calibration (see Mohtadi et al., 2014, for details). The resulting (1σ) errors are on average 1.02°C for the SST estimates.

Palaeo-Mg/Ca SST estimates on such long-time scales require an adjustment for temporal changes in seawater Mg/Ca. Seawater Mg/Ca has not been constant over time due to changes in the hydrologic cycle, hydrothermal activity, continental weathering, and carbonate sedimentation and the dolomite cycle (e.g., Evans & Müller, 2012; Stanley & Hardie, 1998). To account for past seawater Mg/Ca changes, we adjusted our Mg/Ca SST estimates for changes in Cenozoic seawater Mg/Ca by following the approach of Sosdian et al. (2020). This approach uses the same *T. sacculifer* Mg/Ca-temperature calibration as we used

to calculate SST estimates but applies a power constant of 0.41 (Evans & Müller, 2012). It has been shown that a power constant function best describes the combined influence of temperature and seawater Mg/Ca changes on foraminiferal Mg/Ca ratios on long timescales (Hasiuk & Lohmann, 2010). This approach uses a modern day seawater Mg/Ca value of 5.2 mmol/mol and a value of 3.43 mmol/mol based on fluid inclusions for the middle Miocene (Horita et al., 2002) in calculating palaeotemperatures. SST estimates were then calculated using the equation from Sosdian et al. (2020): Mg/Ca (mmol/mol) = 0.293 exp (0.090 × T [°C]).

2.3. Seawater $\delta^{18}O$ Estimates

The combined approach of measuring shell Mg/Ca and stable oxygen isotopes on *T. sacculifer-quadrilobatus* allows to reconstruct temperature independent seawater $\delta^{18}O$ variations. To calculate the $\delta^{18}O$ of seawater ($\delta^{18}O_{sw}$), first, the temperature driven component of changes in the planktic foraminiferal $\delta^{18}O$ record was removed using Mg/Ca palaeothermometry to independently constrain SSTs, including an adjustment for changes in Mg/Ca seawater (Sosdian et al., 2020). The $\delta^{18}O$-temperature relationship of Bemis et al. (1998) was then used to solve for $\delta^{18}O_{sw}$: $\delta^{18}O_{sw}$ (standard mean ocean water, SMOW ‰) = (T[°C] − 16.5 + 4.8 * $\delta^{18}O_{calcite}$ Vienna Pee Dee belemnite (VPDB) ‰)/4.8 + 0.27. The values were converted to standard mean ocean water (SMOW) by adding 0.27%. Second, an estimate of the middle-late Miocene (16–11 Ma) ice-volume signal was subtracted from our $\delta^{18}O_{sw}$ record in order to examine relative variations in local $\delta^{18}O_{sw}$ (i.e., proxy for local surface water salinity changes). The Holbourn et al. (2018) benthic foraminifera stable oxygen isotope record of the northern South China Sea ODP Site 1146 was used to estimate early to late Miocene changes in ice-volume. We assume that ~70% of the benthic foraminifera oxygen isotope signal during the middle-late Miocene is related to changes in continental ice-volume which is based on combined benthic foraminiferal Mg/Ca temperatures and $\delta^{18}O$ analyses (Shevenell et al., 2008). The local $\delta^{18}O_{sw}$ which provides an approximation of relative changes in local surface water salinity during the Early to Late Miocene was then calculated by subtracting 70% of the ODP Site 1146 benthic foraminifera record after normalizing the benthic record to its average value (see Steinke et al., 2010). The errors in $\delta^{18}O_{sw}$ are estimated by propagating the error introduced by the planktic foraminiferal $\delta^{18}O$ and Mg/Ca measurements, the Mg/Ca-temperature calibration, and the $\delta^{18}O$-temperature relationship. The resulting errors (1σ) are on average 0.23‰ for $\delta^{18}O_{sw}$.

2.4. Carbonate Preservation

The carbonate preservation of the planktic foraminifera used for trace element and stable isotope analyses was evaluated by assessing the degree of planktic foraminiferal fragmentation (Thunell, 1976). Samples of the >150 μm size fraction were split using a micro-splitter into representative aliquots containing ≥300 components; whole planktic and benthic foraminifera, planktic and benthic fragments, and other biogenic and lithogenic components were counted (Figure 4e). Planktic foraminiferal fragmentation is expressed as F % = (F/(F + W) * 100, where F is the total number of planktic foraminiferal fragments and W is the total number of whole planktic foraminifera in the sample (Thunell, 1976). In addition, we performed SEM-EDAX Energy Dispersive X-ray Spectroscopy (EDS) analyses using a Fei Quanta 650 FEG equipped with an EDS spectrometer (Octane Elect SDDs) at the State Key Laboratory of Marine Environmental Science (MEL), Xiamen University, in order to investigate potential diagenetic overprinting and alterations which might affect our Mg/Ca and Ba/Ca analyses. Prior to SEM analysis, complete *T. sacculifer-quadrilobatus* tests and tests, which were partly broken into large fragments were cleaned three times with ultrapure water in an ultrasonic bath in order to remove clay particles and carbonate debris (e.g., coccoliths) attached to the tests. After drying the samples at 50°C, the test and test fragments were mounted on SEM stubs and were gold coated.

2.5. Statistical Transition Point Estimation

In order to estimate the timing of transitions in our proxy records for salinity and river/continental runoff, we fitted continuous piecewise regression lines with up to two breakpoints through our local seawater $\delta^{18}O$ and Ba/Ca data, using the R package "segmented" (Muggeo, 2008). The regression models were estimated using the algorithm for breakpoint analysis as described in Muggeo (2003).

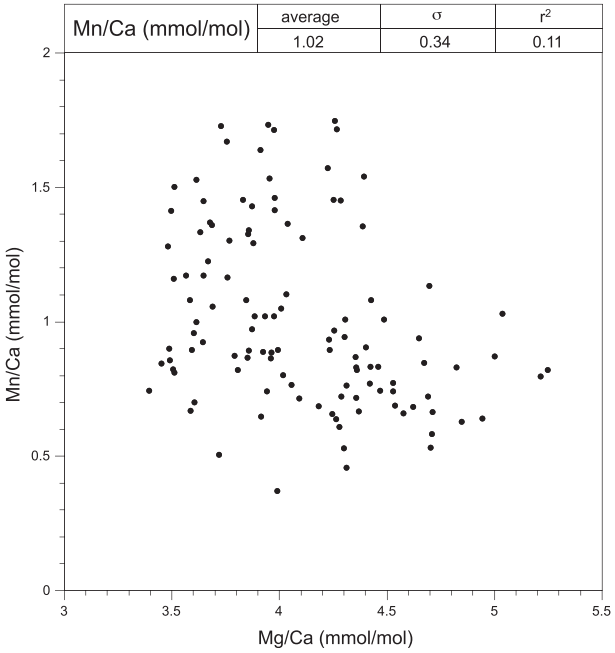

Figure 3. *T. sacculifer-quadrilobatus* Mg/Ca results of Site NGHP-01-01A plotted versus Mn/Ca for the time interval ~16–11 Ma. The absence of a correlation ($R^2 = 0.11$) between Mn/Ca and Mg/Ca indicates that possible Fe-Mn-oxyhydroxides and/or Fe-Mn carbonates present on the foraminiferal shells have no influence on the Mg/Ca ratios.

3. Results

3.1. The Potential Influence of Diagenetic Overprinting on the Planktic Foraminiferal Mg/Ca and Ba/Ca Ratios

Clay contamination (e.g., Barker et al., 2003) and the occurrence of syn-sedimentary and post-depositional Mn-oxyhydroxides and/or Mn-rich carbonate coatings (e.g., Pena et al., 2005) precipitated on the foraminiferal shells can affect the Mg/Ca ratios. Those coatings can contain additional Mg resulting in overestimated temperatures due to higher Mg/Ca ratios. Barker et al. (2003) noted that contamination may occur when Al/Ca and Mn/Ca ratios exceed 0.1 mmol/mol. For that reason, Al/Ca and Mn/Ca were determined in conjunction with Mg/Ca to assess the effectiveness of the cleaning procedure and the occurrence of syn-sedimentary and post-depositional Mn-oxyhydroxides and/or Mn-rich carbonate coatings, respectively. The measurements reveal that Al concentrations are under the detection limit of the ICP-MS techniques, indicating no Mg contribution by clays. Mn/Ca ratios of the analyzed samples varied between 0.37 and 1.94 mmol/mol. These values are distinctly higher than the 0.1 mmol/mol Mn/Ca ratios given by Barker et al. (2003) for clean, uncontaminated foraminiferal tests from recent sediments (Figure 3). However, those Mn/Ca values are similar to those of Miocene planktic foraminiferal samples of ODP Site 1146 from the northern South China Sea and other Plio-Miocene records (e.g., Steinke et al., 2010). Although the Mn/Ca ratios exceed 0.1 mmol/mol, which might indicate the presence of and Mn-rich coatings, there is no relationship ($r^2 = 0.11$) between Mg/Ca and Mn/Ca (Figure 3). Therefore, it is suggested that the Mg/Ca ratios are not affected by the occurrence of syn-sedimentary and post-depositional precipitated Mn-oxyhydroxides and/or Mn-rich carbonate coatings (see also Steinke et al., 2010). A unique problem for Ba/Ca analysis could be the presence of sedimentary barite ($BaSO_4$; e.g., Lea & Boyle, 1991). With a few exceptions of values ranging between ~2 and 4.56 μmol/mol (Figure 4h), which might reflect overprinted Ba/Ca ratios, our Ba/Ca ratios are generally similar to those of core SK237-GC04 off the Malabar (southwest) coast of India (Saraswat et al., 2013) suggesting that the Ba/Ca ratios are not contaminated by sedimentary barite coatings. In addition, the EDAX-EDS analyses do not reveal any crystal overgrowth and coatings rich in Ba, suggesting that our Ba/Ca ratios are not affected by the occurrence of sedimentary barite crystal coatings.

3.2. Mg/Ca-SST Estimates

The *T. sacculifer-quadrilobatus* Mg/Ca ratios from NGHP-01-01A vary between 3.95 and 5.25 mmol/mol (Figure 4b). Our resulting Mg/Ca-SST estimates reveal temperatures around ~27.7°C between ~16 and 15 Ma. This period is followed by a distinct cooling to ~25.8°C between ~15 and 14.8 Ma. Highest SSTs (~29.1°C) are recorded between ~14.8 and 14.4 Ma. After ~14 Ma, temperatures decrease from ~28.3°C at ~14 Ma to 25.8°C at ~13.6 Ma (Figure 4c). The decrease in SSTs is followed by a period (~13.6 Ma to 11 Ma) of relatively constant SSTs of around 26.8°C (Figure 4c). The adjusted Mg/Ca SST estimates for secular changes in seawater Mg/Ca results are in average 1.9°C warmer than those estimated without a correction for changes in seawater Mg/Ca (Figure 4d). Although the absolute Mg/Ca-based SST estimates may be affected by temporal variations in seawater Mg/Ca during the Miocene, we suggest that the amplitude, trend and timing of our inferred SST changes are not affected as shown by the approach to account for past seawater Mg/Ca changes (Figure 4d). The relative changes in SST are thus considered to represent a reliable approximation of relative changes in EAS SSTs during the middle to late Miocene.

3.3. Stable Oxygen Isotopes

$\delta^{18}O$ values of *T. sacculifer-quadrilobatus* vary between −1.28‰ and −2.91‰ between ~16 and 11 Ma (Figure 4a). The $\delta^{18}O$ record shows a long-term gradual decrease in $\delta^{18}O$ from ~16 to 10 Ma. A prominent change in $\delta^{18}O$ from ~−1.82‰ to −2.21‰ occurs at ~14.2 Ma that is followed by a gradual decrease toward

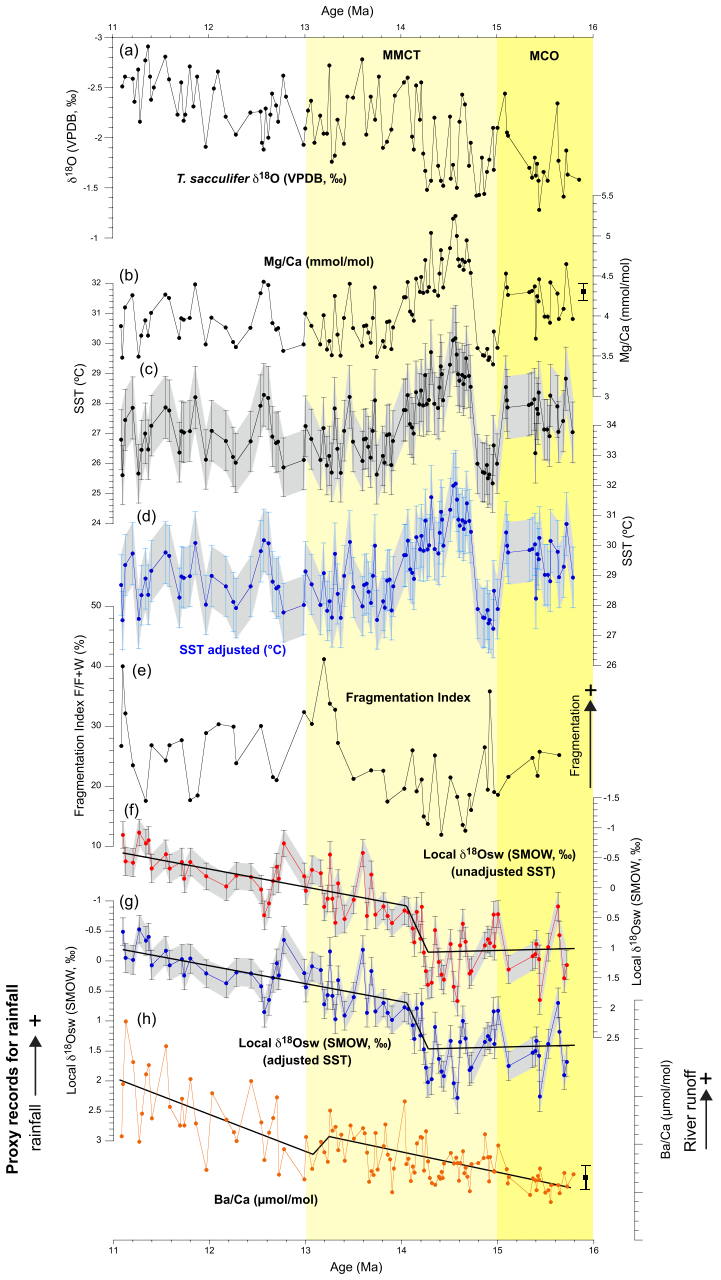

Figure 4. (a) Oxygen isotope record of *T. sacculifer-quadrilobatus* of Site NGHP-01-01A, (b) Mg/Ca ratios (mmol/mol) of *T. sacculifer-quadrilobatus*, and (c) Mg/Ca SST estimates. SST (°C) estimates (black) were obtained by using the species-specific equation for *T. sacculifer* (Anand et al., 2003; Mg/Ca [mmol/mol] = 0.347 exp [0.090 × T, °C]). (d) Mg/Ca SST estimates adjusted for changes in seawater Mg/Ca by following the approach of Sosdian et al. (2020; blue). Bars and envelopes in (d) and (e) indicate 1σ errors. (e) Carbonate preservation at Site NGHP-01-01A as expressed by the planktic foraminiferal fragmentation index (Thunell, 1976). (f and g) Local seawater $\delta^{18}O$ estimates at NGHP-01-01A. Local seawater $\delta^{18}O$ was derived by removing the temperature (f, using unadjusted Mg/Ca SST estimates for changes in seawater Mg/Ca, red; g, using adjusted Mg/Ca SST estimates for changes in seawater Mg/Ca, blue), driven component of changes in the planktonic foraminiferal $\delta^{18}O$ using the Bemis et al. (1998) $\delta^{18}O$:temperature equation and changes in global ice volume (see text for details). Bars and envelopes in (f) and (g) indicate 1σ errors (h) *T. sacculifer-quadrilobatus* Ba/Ca ratios. The analytical error of the Mg/Ca and Ba/Ca measurements was determined by combining the relative standard deviations for the in-house standard and replicate measurements. The 1σ errors of the $\delta^{18}O_{sw}$ and SST reconstructions are estimated by propagating the error introduced by the planktic foraminiferal $\delta^{18}O$ and Mg/Ca measurements, the Mg/Ca:temperature calibration, and the $\delta^{18}O$:temperature equation. Yellow vertical bars indicate the timing of the Miocene Climatic Optimum (MCO) and the Middle Miocene climate transition (MMCT).

lighter (lower) $\delta^{18}O$ values thereafter (Figure 4a). The benthic foraminifera $\delta^{18}O$ record of *P. wuellerstorfi* and *C. mundulus* reveals values ranging between 0.32‰ and 2.6‰ between ~16 and 11 Ma (Figure 5e). The benthic isotope record of Site NGHP-01-01A reveals the same large increase in benthic foraminiferal isotopes of ~1.0–1.3% between ~16 and 12.5 Ma, which has also been reported for other Miocene benthic isotope records (e.g., Flower & Kennett, 1994; Holbourn et al., 2013). However, our benthic record does not show the step-like increase in benthic $\delta^{18}O$, such as the sharp increase in $\delta^{18}O$ at ~13.9 Ma (e.g., Holbourn et al., 2013; Shevenell et al., 2004). We attribute this to the rather low temporal resolution of our benthic isotope record because of insufficient specimens for isotope analyses in many samples. Our record reveals a pronounced decrease in $\delta^{18}O$ between ~15 and 14.8 Ma, which has not been reported previously and is most likely attributed to regional changes in hydrography (Figure 5e). The large increase in benthic foraminiferal $\delta^{18}O$ of ~1.0–1.3% between ~16 and 12.5 Ma suggests that our benthic oxygen isotope curve records the middle Miocene expansion of the Antarctic ice sheet and Southern Hemisphere ocean surface water cooling (e.g., Holbourn et al., 2013, 2018).

3.4. Local $\delta^{18}O$ of Seawater

The local $\delta^{18}O_{sw}$ reconstructions using the unadjusted Mg/Ca-based SST estimates reveal values varying between ~−0.82‰ and 1.99‰ between ~16 and 11 Ma (Figure 4f). The local $\delta^{18}O_{sw}$ estimates reveal a prominent shift toward lower (lighter) local $\delta^{18}O_{sw}$ values at around ~14.2 Ma (Figure 4f). The $\delta^{18}O_{sw}$ estimates show a gradual decrease after ~14 Ma (Figure 4f), indicating an increasing freshening of the EAS. The local $\delta^{18}O_{sw}$ estimates using Mg/Ca-based SST adjusted for secular changes in seawater Mg/Ca are on average 0.39‰ heavier than those calculated without a correction for changes in seawater Mg/Ca (Figure 4g). Although the absolute local $\delta^{18}O_{sw}$ values are different, the trend and timing of both approaches (unadjusted vs. adjusted Mg/Ca-based SST estimates) are identical (Figures 4f and 4g). We consider the relative changes in our local $\delta^{18}O_{sw}$ estimate therefore as a reliable approximation of relative changes in local $\delta^{18}O_{sw}$ in the EAS during the middle to late Miocene. Statistical analysis of breakpoints in the local $\delta^{18}O_{sw}$ data using the R package "segmented" (Muggeo, 2008; Figures 4f and 4g) indicates a pair of breakpoints at 14.04 ± 0.11 Ma (1σ) and 14.27 ± 0.08 Ma, forming a distinct step function/regime change. The two breakpoint model is highly significant when compared by F test to a model with no breakpoints ($F = 5.90$, $df = 4$, $p < 0.001$).

3.5. Ba/Ca Ratios

T. sacculifer-quadrilobatus Ba/Ca ratios from Site NGHP-01-01A vary between 0.79 and 4.56 μmol/mol (Figure 4h). Ba/Ca ratios rise gradually from values of ~1.2 μmol/mol at around 16 Ma to maximum values of 4.56 μmol/mol at 11 Ma (Figure 4h). The Ba/Ca record shows an overall gradual increase in Ba/Ca from ~16 to 11 Ma, most likely reflecting a gradual increase in riverine runoff and thus an increase in monsoonal rainfall. The statistical analysis of breakpoints in the local $\delta^{18}O_{sw}$ data using the R-package "segmented" reveal no breakpoints around 14 Ma (Muggeo, 2008; Figure 4h). A single breakpoint was identified at 11.97 ± 0.39 Ma, but this single breakpoint model was not significant when compared to a model with no breakpoints ($F = 2.67$, $df = 2$, $p > 0.05$, Figure 4h).

3.6. Carbonate Preservation

The planktic foraminiferal fragmentation index yields values that vary between 12% and 42% (Figure 4e). As a planktic foraminiferal test fragmentation index below 50% is considered to indicate no significant carbonate dissolution, this suggests that the planktic foraminiferal shells are well preserved at Site NGHP-01-01A. We suggest that the high clay content of the sediment at Site NGHP-01-01A might have helped to reduce corrosiveness of pore waters to prevent post-depositional dissolution. The SEM analyses reveal neither crystal overgrowth, coatings, or crusts on the outer tests nor any thin smooth layer or tiny patina at the innermost part of the tests. The wall texture images reveal a very well preserved, unaltered biogenic texture without any fine or coarse-grained crystallites (Figure 6). The primary wall structure and the spine holes as well as spine cavities are well preserved. SEM images on the shell outer surface of *T. sacculifer-quadrilobatus* show that the spine holes and primary wall texture are partly obscured by gametogenic calcite (GAM calcite; Figure 6). In addition, we found no evidence of a "frosty" wall texture in the sense of the Sexton et al. (2006) study. We therefore conclude that the variations in foraminiferal Mg/Ca during the Middle to Late Miocene are primarily driven by changes in the ambient water temperature rather than by post-depositional, partial dissolution or diagenetic alterations.

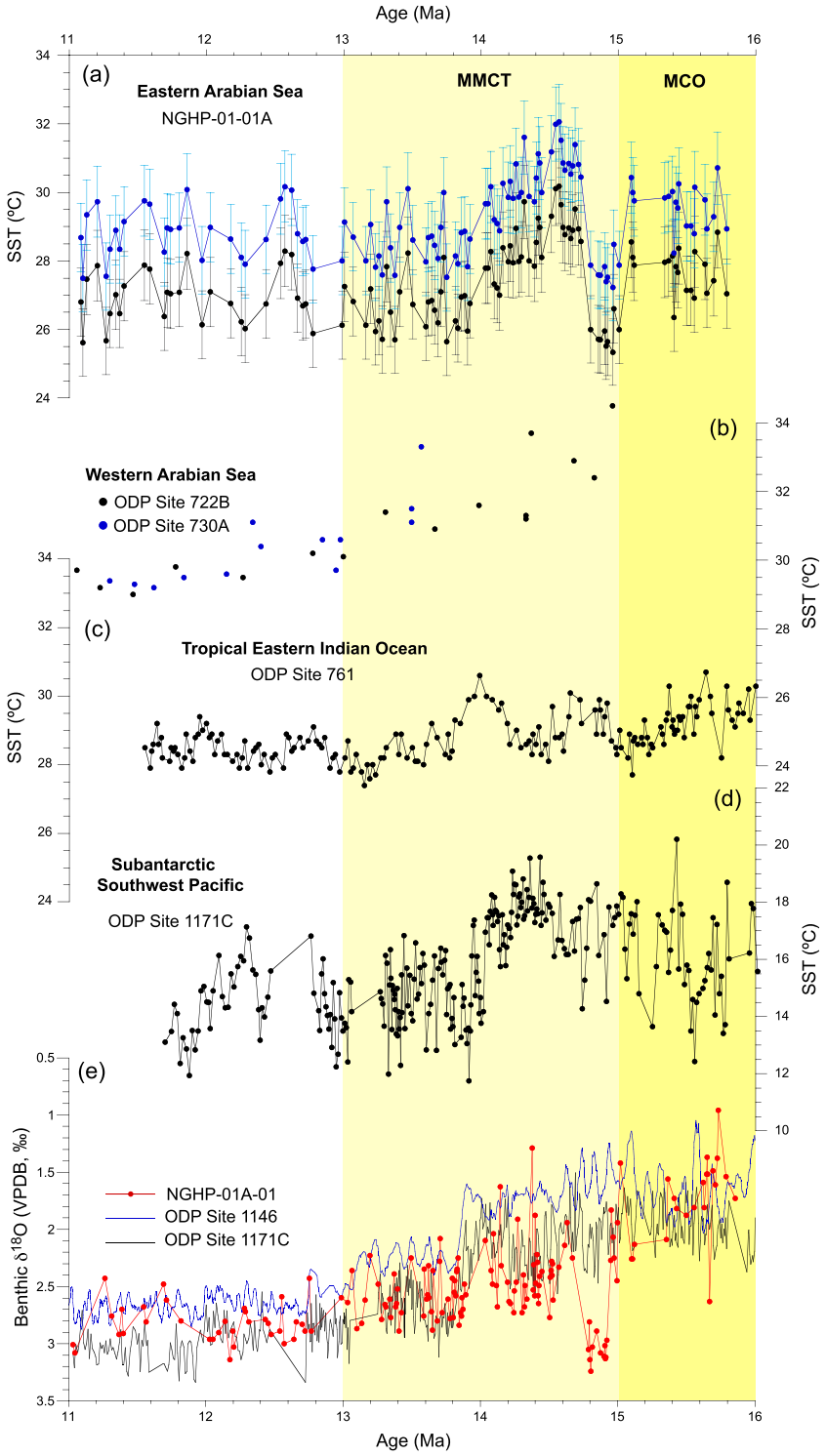

Figure 5. (a) Sea surface temperature (SST) estimates derived from planktic foraminiferal Mg/Ca at Site NGHP-01A-01; SST estimates unadjusted (black) and adjusted (blue) for changes in seawater Mg/Ca, bars in (a) indicate 1σ errors, (b) TEX86 SST estimates of ODP Sites 722B and 730A from the Western Arabian Sea (Zhuang et al., 2017), (c) Mg/Ca-based SST estimates of ODP Site 761 of the tropical Eastern Indian Ocean (Sosdian et al., 2020), and (d) Mg/Ca-based SST estimates of ODP Site 1171C from the subantarctic Southwest Pacific (Shevenell et al., 2004). (e) Benthic foraminiferal $\delta^{18}O$ records of ODP Site 1146 (5-point running average blue; Holbourn et al., 2018), ODP Site 1171C (black; Shevenell et al., 2004), and Site NGHP-01-01A (red; this study). Yellow vertical bars indicate the timing of the Miocene Climatic Optimum (MCO) the Middle Miocene climate transition (MMCT).

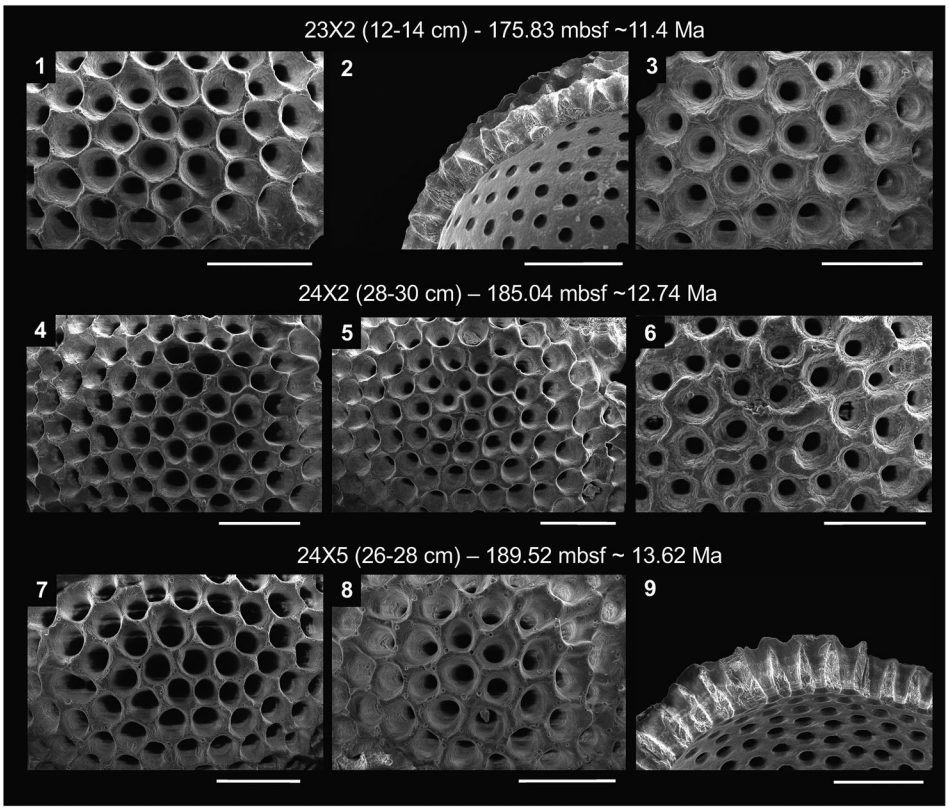

Figure 6. Detailed SEM images of the wall textures of *T. sacculifer-quadrilobatus* from Site NGHP-01-01A samples. Images reveal neither any crystal overgrowth, coatings, or crusts on the outer tests nor any thin smooth layer or tiny patina at the innermost part of the tests (1, 4, 5, 7, and 8). The primary wall structure, the spine holes, and the spine cavities are well preserved (2 and 9). The shell outer surface of *T. sacculifer-quadrilobatus* show that the spine holes and primary wall texture are partly obscured by gametogenic calcite (GAM calcite; 3 and 6) scale bars: 1, 2, 4, 5 = 50 μm; 3, 6 = 40 μm.

4. Discussion

4.1. SST Variability in the EAS During the Middle to Late Miocene

The major features of our EAS SST record are a distinct cooling between ~15 and 14.8 Ma and highest SSTs are recorded between ~14.8 and 14.4 Ma (Figures 4c, 4d, and 5a). An ~2.5°C decrease in temperature occurred between ~14 and ~13.6 Ma from the warmest EAS SSTs between ~14.8 and 14.4 Ma to cooler temperatures after 13.6 Ma (Figures 4c, 4d, and 5a). Our EAS SST record shares similarities in patterns and trends with the TEX_{86}-based SST records at ODP Sites 722B and 730A from the WAS (Zhuang et al., 2017; Figure 5b), the ODP Site 761 Mg/Ca-based SST record from the tropical Eastern Indian Ocean (Sosdian et al., 2020; Figure 5c) and with the ODP Site 1171C Mg/Ca-based SST record from the subantarctic Southwest Pacific (Shevenell et al., 2004; Figure 5d), which all indicate a cooling trend during the middle Miocene climate transition (MMCT). The decrease in SST at our Site between ~14 and ~13.6 Ma coincides (within the uncertainties of the individual age models) with a major increase in the benthic $\delta^{18}O$ at ~13.9 Ma, which is attributed to a major phase of glacial Antarctic cryosphere expansion and/or deep water cooling (Holbourn et al., 2013, 2018; Figure 5e). We therefore suggest that SST changes in the EAS were affected by Southern Hemisphere high-latitude climate change (see discussion below).

4.2. Seawater $\delta^{18}O$ and Ba/Ca Variations in the EAS Region During the Middle to Late Miocene

Our Ba/Ca record shows a long-term gradual increase, most likely reflecting an increase in riverine runoff and thus an intensification in monsoonal rainfall from ~15 to 11 Ma (Figures 4h and 8b). Different to the long-term increasing trend in the Ba/Ca record, the decrease in local seawater $\delta^{18}O$ estimates is initiated by a notable freshening in the EAS at ~14.2 Ma (Figures 4f, 4g, and 8a). This pronounced shift toward

lower salinity surface waters is not evident from the Ba/Ca record. We suggest that the long-term increase in Ba/Ca ratios and $\delta^{18}O_{sw}$ is most likely attributable to a gradual increase in monsoonal rainfall in West India and the adjacent EAS leading to increased river runoff from the Western Ghats during the middle to late Miocene. Whereas the planktic foraminiferal Ba/Ca estimates serve as a direct recorder of changes in continental runoff and thus changes in continental monsoonal rainfall, our local seawater $\delta^{18}O$ estimates reflect not only the effects of an increase in monsoonal rainfall in West India but also hydrographic changes in water masses explaining the different nature of the two records (Figures 4f–4h). Several hydrographic changes in water masses, alone or together, might have led to the pronounced freshening of the EAS at around ~14.2 Ma as evident from our local $\delta^{18}O_{sw}$ estimates:

1. The intrusion of low-salinity water from the BoB during winter related to summer runoff of the Ganga-Brahmaputra river system, which reached the EAS during the winter season. Although the Indian subcontinent was located somewhat closer to the equator, the Indian Ocean ocean-continent distribution was close to its modern configuration by ~14 Ma (Scotese, 2002). As the paleogeography was similar to today and the SAM was operating at least since the late Eocene (e.g., Huber & Goldner, 2012; Licht et al., 2014), we suggest that the present day monsoon-driven surface water circulation patterns likely existed already during the early/middle Miocene. For that reason, it is possible that part of the freshening at our site at ~14 Ma could be attributed to an intrusion of lower salinity water from the Eastern Indian Ocean related to increased summer runoff of the Ganga-Brahmaputra river system into the BoB due to a stronger SAM rainfall over the Indian subcontinent and the BoB region after ~14 Ma (Hormann et al., 2019; Prasanna Kumar et al., 2004).
2. The shoaling and final closure of the Miocene Indian Ocean Gateway ("Tethyan Seaway or Mesopotamian Seaway") to the Mediterranean around ~14 Ma. The MMCT was also the time when the final closure of the Tethyan Seaway to the Mediterranean occurred, which resulted in the termination of the inflow of warm and salty waters of the Tethyan Indian Saline Waters (TISW) from the Mediterranean Sea into the Arabian Sea (Bialik et al., 2019). The closure of the Tethyan seaway coincides with the freshening in the EAS around that time. Bialik et al. (2019) suggest that the TISW advection may have affected the whole Arabian Sea and the eastern African Margin. Under this scenario, our site may have been influenced by warm and saline TISW before ~14 Ma, although its higher density may have prevented an impact on the surface waters in our study area similar to the modern Persian Gulf Water (PGW) mass (Prasad et al., 2001).
3. Changes in the oceanography of the Indian and Southern Ocean associated the with final closure of the Tethys seaway. Model simulations reveal that the closure of the Tethyan seaway and the termination of TISW production induce strong changes in the latitudinal density gradient and a strengthening of the Antarctic Circumpolar Current (ACC; Hamon et al., 2013). A strengthening of the ACC results in lower SSTs, an increase in sea ice extent and a stronger latitudinal thermal gradient, and thus a strengthening of the westerlies (Hamon et al., 2013). A strengthening of the ACC is also associated with a gradual freshening of the surface waters between 14.2 and 13.8 Ma at ODP Site 1171C in the subantarctic Southwest Pacific (Shevenell et al., 2004; Figure 7b). The notable pronounced freshening in the Arabian Sea (~14.2 Ma) coincides with the freshening in the ACC region (Figure 7b). We therefore suggest that the pronounced shift in $\delta^{18}O_{sw}$ at ~14 Ma may have been induced by Southern Hemisphere high-latitude climatic and hydrographic changes. Our data imply that Southern Ocean Intermediate Waters (SOIW) may have transmitted the changes in salinity to the Arabian Sea via an "oceanic tunnel" mechanism (Liu & Yang, 2003; Pena et al., 2013). After subducting and spreading northward into the Indian Ocean, the SOIW forms the Indian Ocean Central Water (IOCW), which reached the surface in the WAS and southwestern EAS upwelling regions affecting the salinity patterns at our Site NGHP-01-01A (You, 1998) as was previously also shown for other locations in the Indian Ocean (e.g., Kiefer et al., 2006; Mohtadi et al., 2010; Romahn et al., 2014).

4.3. Controls on Rainfall Intensification During the Middle Miocene

The general pattern of the Ba/Ca and $\delta^{18}O_{sw}$ changes is interpreted to reflect a notable progressive increase in SAM rainfall intensity from at least ~15 to 11 Ma. The proposed increase in rainfall intensity in the SAM region occurred during a time period (the MMCT —~15–13 Ma) when Earth's climate changed from a warmer phase with a reduced Antarctic ice sheet to a colder phase with more permanently glaciated

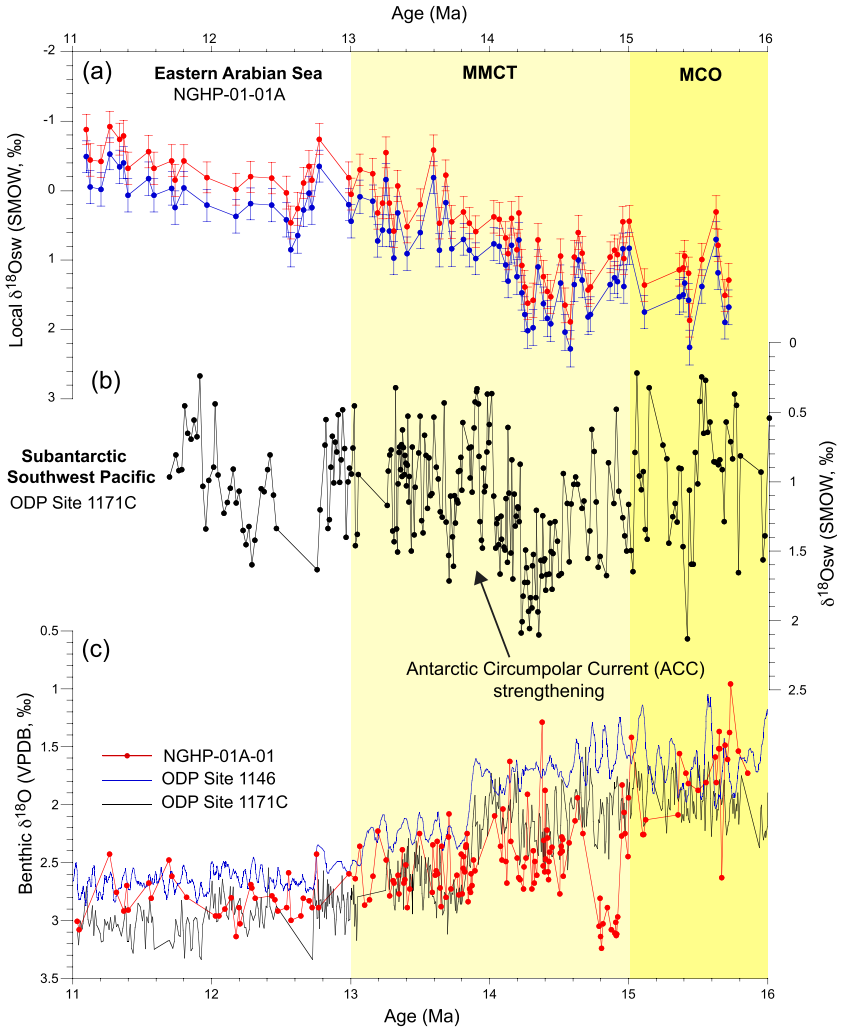

Figure 7. (a) Local seawater $\delta^{18}O$ estimates at Site NGHP-01-01A calculated using unadjusted (red) and adjusted (blue) Mg/Ca SST estimates for changes in seawater Mg/Ca; bars in (a) indicate 1σ errors. (b) Seawater $\delta^{18}O$ estimates of ODP Site 1171C from the subantarctic Southwest Pacific (Shevenell et al., 2004). (c) Benthic foraminiferal $\delta^{18}O$ records of ODP Site 1146 (5-point running average blue; Holbourn et al., 2018), ODP Site 1171C (black; Shevenell et al., 2004), and Site NGHP-01-01A (red; this study). Yellow vertical bars indicate the timing of the Miocene Climatic Optimum (MCO) and the Middle Miocene climate transition (MMCT).

conditions. This prominent transition was most likely caused by a decline in global atmospheric CO_2 (Zachos et al., 2008; Zhang et al., 2013) or by a change in orbital forcing (Holbourn et al., 1995). The expansion of the Antarctic ice sheets from ~14.2 to 13.8 Ma and the ongoing expansion of sea ice into the late Miocene is suggested to have changed the global atmospheric circulation, including the strength and position of the southern hemisphere Westerly Winds (e.g., Groeneveld et al., 2017) and the Intertropical Convergence Zone (ITCZ; e.g., Holbourn et al., 2010), and thus wind and rainfall patterns. Whereas the majority of proxy records for summer SAM wind strength indicate that the summer SAM wind system intensified after ~12.9 Ma (e.g., Betzler et al., 2016; Gupta et al., 2015; Figures 8d and 8e), the studies of Kroon et al. (1991) and Bialik et al. (2020) suggest an earlier intensification of the SAM wind between ~14.8 and 14.0 Ma (Figure 8c). The strengthening of the SAM wind system prior to 12.9 Ma is consistent with an already summer SAM at around 15 Ma as inferred from our Ba/Ca record (Figure 8b). The gradual intensification of SAM rainfall after ~15 Ma would also fit with the proposed northward movement of the southern Westerly Winds and the Hadley cell in the Indian Ocean from the Middle to the Late Miocene (Groeneveld et al., 2017) and the resulting strengthening of the cross-equatorial Somali

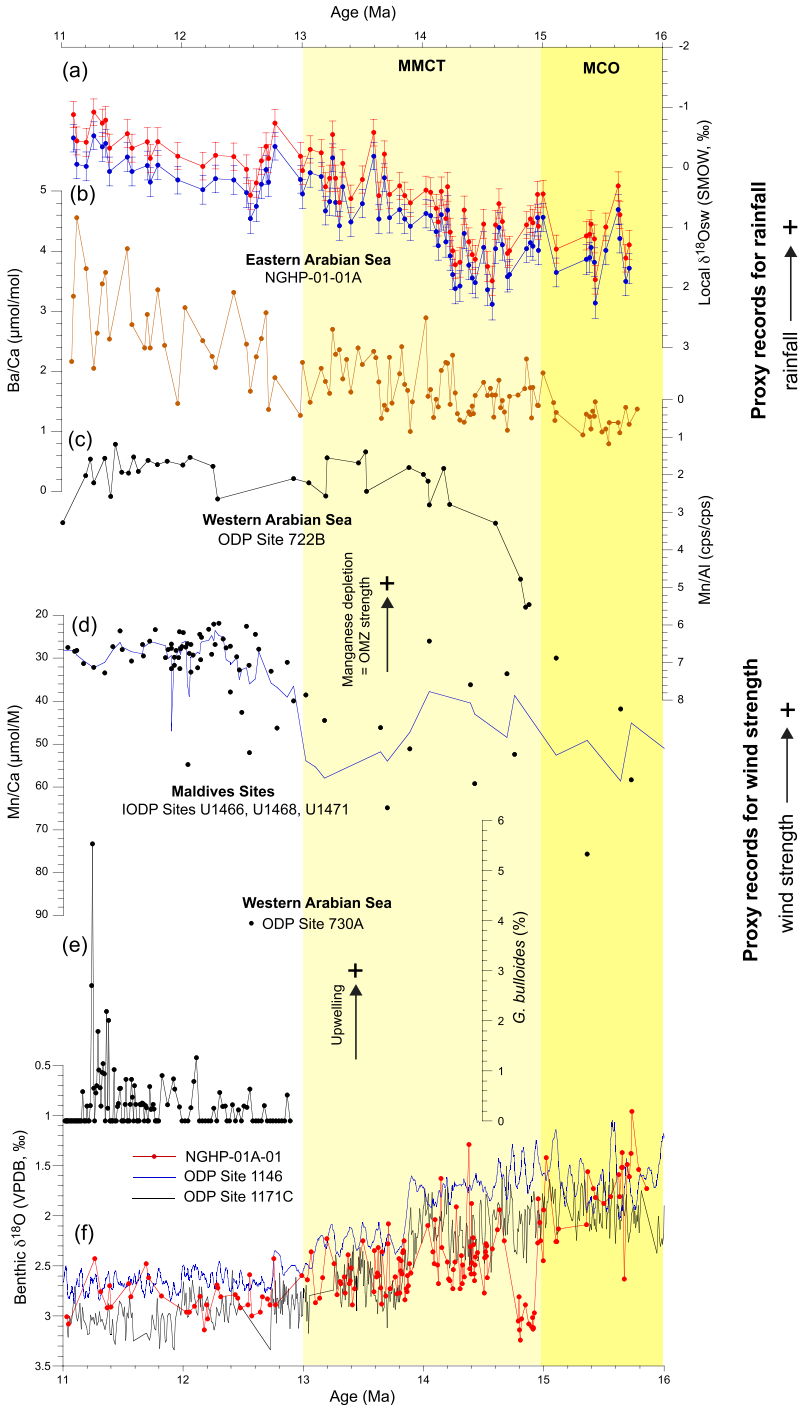

Figure 8. Comparative proxy records of the South Asian monsoon (SAM) since the early Miocene. (a) Local seawater $\delta^{18}O$ estimates of Site NGHP-01-01A from the Eastern Arabian Sea calculated using unadjusted (red) and adjusted (blue) Mg/Ca SST estimates for changes in seawater Mg/Ca; bars in (a) indicate 1σ errors; (b) Ba/Ca ratios of Site NGHP-01-01A from the Eastern Arabian Sea; (c) Mn/Al record of ODP Site 722B from the Western Arabian Sea, indicative of Oxygen Minimum Zone fluctuations (OMZ; Bialik et al., 2020); (d) Mn/Ca record from the Maldives Inner Sea, indicative of Oxygen Minimum Zone fluctuations (OMZ; Betzler et al., 2016; blue line: 3-point running average); and (e) *G. bulloides* abundance of ODP Site 730A (Gupta et al., 2015) from the Western Arabian Sea. (f) Benthic foraminiferal $\delta^{18}O$ records of ODP Site 1146 (5-point running average blue; Holbourn et al., 2018), ODP Site 1171C (black; Shevenell et al., 2004), and Site NGHP-01-01A (red; this study). Yellow vertical bars indicate the timing of the Miocene Climatic Optimum (MCO) and the Middle Miocene climate transition (MMCT).

Jet during the middle Miocene (Betzler et al., 2016; Bialik et al., 2020). This led to a progressive global reorganization of the atmospheric circulation as a result of increasing latitudinal thermal gradients during the MMCT. An increasing SAM during the middle Miocene may also explain a stronger westerly jet stream over Central Asia during and after the MMCT (Frisch et al., 2019). Modern observations show that a stronger than average summer SAM strengthens the westerly jet stream north of the Tibetan Plateau (Schiemann et al., 2009).

Climate modeling studies suggest that the surface uplift of the Himalayan-Tibetan Plateau is also a crucial parameter for the onset and intensification of the Asian monsoons during the Cenozoic (e.g., Farnsworth et al., 2019; Zhang et al., 2015). The numerical simulations show a distinct increase in mean annual precipitation in the East Asian monsoon (EAM) region between 14.9 and 9.4 Ma as a response to the uplift of the Himalayan-Tibetan region with little influence from atmospheric CO_2 (Clark et al., 2005; Farnsworth et al., 2019; Ouimet et al., 2010). Likewise, numerical simulations reveal that in particular the uplift of the eastern and western Tibetan Plateau has important effects on the strengthening of the SAM rainfall (Zhang et al., 2015). The strengthening in SAM rainfall from ~15 to 11 Ma based on our proxies is therefore consistent with recent general circulation model simulations of the monsoon evolution (Farnsworth et al., 2019; Zhang et al., 2015). Although the uplift of the Himalayan-Tibetan region has been identified as one of the main drivers of the long-term evolution and development of the EAM and SAM (see above), climate models also show the importance of the zonal heat gradient/thermal contrast between the land and sea near South Asia for the evolution of the SAM compared to the EAM (Liu & Yin, 2002). Likewise, it was suggested that the SAM is strengthened because of the combined effect of the Himalayan uplift that acts as a thermal barrier for the westerlies and for changes in surface heat fluxes from the non-elevated regions of the Indian landmass (Boos & Kuang, 2013). We thus suggest that the intensification of the SAM during the middle Miocene could have been caused by a combination of the ongoing uplift of the Himalayan-Tibetan region and changes in the ocean-atmospheric circulation related to decreasing atmospheric CO_2, changes in orbital forcing, and the progressive cryosphere expansion on Antarctica. Although our SAM rainfall record does not cover the complete time interval of the MCO, our rainfall reconstructions together with climate model simulations for the EAM (Farnsworth et al., 2019) suggest that Asian monsoonal rainfall was weaker during the MCO compared to the later part of the middle/late Miocene, but that does not exclude that it may still have been stronger than today's monsoon.

5. Conclusions

Our new reconstruction of hydrological changes related to the SAM shows a notable progressive increase in SAM rainfall intensity during the MMCT. The rainfall reconstruction reflects an already intensifying summer SAM at around 15 Ma which is in good agreement with an intensification of the SAM wind between ~14.8 and 14.0 Ma. Our planktic foraminiferal Ba/Ca estimates reveal changes in continental runoff from the Western Ghats and thus an intensification in monsoonal rainfall in West India and the adjacent EAS from at least ~16 to 11 Ma. A further SAM intensification during the middle Miocene is consistent with recent model simulations and fits well into the picture of an overall strengthening and expanding monsoon from the Eocene to middle/late Miocene. This could be attributed to the gradual uplift of the Himalayan-Tibetan Plateau followed by an acceleration after the MMCT related to changing atmospheric CO_2, orbital forcing, and glaciation on Antarctica. Our seawater $\delta^{18}O$ estimates, on the other hand, reflect the combined effect of local runoff and rainfall and, oceanic advection due to Southern Hemisphere high-latitude climate and hydrographic changes. The prominent decrease in seawater $\delta^{18}O$ at ~14 Ma suggests that SOIW may have transmitted subantarctic salinity changes into the Arabian Sea via an "oceanic tunnel" mechanism. Our proxy records display a combination of different controlling factors, which are local runoff, rainfall, and oceanic advection. Our study further demonstrates that the combined usage of Ba/Ca and $\delta^{18}O$ represents a valuable method to fully capture different impacts on the hydrography and climate in a monsoonal setting.

Data Availability Statement

Data of this manuscript are archived at PANGAEA-Data Publisher for Earth and Environmental Science and can be downloaded using the following link (https://doi.org/10.1594/PANGAEA.910403).

Acknowledgments

This study has been funded by the National Natural Science Foundation of China through a grant to S. Steinke (NSFC grant No. 41776055) and Z. Jian and S. Steinke (NSFC grant No. 919582080). We express our gratitude to H. Kuhnert (MARUM, University of Bremen) and his team for stable isotope analyses. We thank P. Qiao (Tongji University Shanghai) for technical and analytical support with the ICP-MS analyses, A. Dolman (Alfred-Wegener-Institute, Helmholtz Centre for Polar and Marine Research, Potsdam, Germany) for statistical analyses, and B. Wang (State Key Laboratory of Marine Environmental Science, Xiamen University) and his team for the SEM-EDAX Energy Dispersive X-ray Spectroscopy (EDS) analyses. L. Giosan acknowledges funding from USSP and WHOI and thanks colleagues and crew from the NGHP-01 expedition for intellectual interactions leading to long-standing interests in the fluvial-continental margin systems of Peninsular India. J. Groeneveld thanks the State Key Laboratory of Marine Environmental Science (Xiamen University) for a MEL Senior Visiting Fellowship (Project No. MELRS1915).

References

An, Z. S., Clemens, S. C., Shen, J., Qiang, X., Jin, Z., Sun, Y., et al. (2011). Glacial-interglacial Indian summer monsoon dynamics. *Science*, *333*(6043), 719–723. https://doi.org/10.1126/science.1203752

Anand, P., Elderfield, H., & Conte, M. H. (2003). Calibration of Mg/Ca thermometry in planktonic foraminifera from a sediment trap time series. *Paleoceanography*, *18*(2), 1050. https://doi.org/10.1029/2002PA000846

Bahr, A., Schönfeld, J., Hofmann, J., Voigt, S., Aurahs, R., Kucera, M., et al. (2013). Comparison of Ba/Ca and $\delta^{18}O_{WATER}$ as freshwater proxies: A multi-species core-top study on planktonic foraminifera from the vicinity of the Orinoco River mouth. *Earth and Planetary Science Letters*, *383*, 45–57. https://doi.org/10.1016/j.epsl.2013.09.036

Barker, S., Greaves, M., & Elderfield, H. (2003). A study of cleaning procedures used for foraminiferal Mg/Ca paleothermometry. *Geochemistry, Geophysics, Geosystems*, *4*(9), 8407. https://doi.org/10.1029/2003GC000559

Behara, A., Vinayachandran, P. N., & Shankar, D. (2019). Influence of rainfall over Eastern Arabian Sea on its salinity. *Journal of Geophysical Research: Oceans*, *124*, 5003–5020. https://doi.org/10.1029/2019JC014999

Bemis, B. E., Spero, H. J., Bijma, J., & Lea, D. W. (1998). Reevaluation of the oxygen isotopic composition of planktonic foraminifera: Experimental results and revised paleotemperature equations. *Paleoceanography*, *13*(2), 150–160. https://doi.org/10.1029/98PA00070

Betzler, C., Eberli, G. P., Kroon, D., Wright, J. D., Swart, P. K., Nath, B. N., et al. (2016). The abrupt onset of the modern South Asian Monsoon winds. *Scientific Reports*, *6*, 29838. https://doi.org/10.1038/srep29838

Bialik, O. M., Auer, G., Ogawa, N. O., Kroon, D., Waldmann, N. D., & Ohkouchi, N. (2020). Monsoons, upwelling, and the deoxygenation of the northwestern Indian Ocean in response to middle to late Miocene global climatic shifts. *Paleoceanography and Paleoclimatology*, *35*, e2019PA003762. https://doi.org/10.1029/2019PA003762

Bialik, O. M., Frank, M., Betzler, C., Zammit, R., & Waldmann, N. D. (2019). Two-step closure of the Miocene Indian Ocean Gateway to the Mediterranean. *Scientific Reports*, *9*, 8842. https://doi.org/10.1038/s41598-019-45308-7

Boos, W. R., & Kuang, Z. (2013). Sensitivity of the South Asian monsoon to elevated and nonelevated heating. *Scientific Reports*, *3*, 1192. https://doi.org/10.1038/srep01192

Campanile, D., Nambiar, C. G., Bishop, P., Widdowsonz, M., & Brown, R. (2008). Sedimentation record in the Konkan-Kerala Basin: Implications for the evolution of the Western Ghats and the Western Indian passive margin. *Basin Research*, *20*, 3–22. https://doi.org/10.1111/j.1365-2117.2007.00341.x

Clark, M. K., House, M. A., Royden, L. H., Whipple, K. X., Burchfiel, B. C., Zhang, X., & Tang, W. (2005). Late Cenozoic uplift of southeastern Tibet. *Geology*, *33*(6), 525–528. https://doi.org/10.1130/G21265.1

Collett, T. S., Riedel, M., Cochran, J. R., Boswell, R., Presley, J., Kumar, P., et al. (2007). National gas hydrate program Expedition 01 initial reports. Directorate general of hydrocarbons, New Delhi.

De Vleeschouwer, D., Vahlenkamp, M., Crucifix, M., & Pälike, H. (2017). Alternating Southern and Northern Hemisphere response to astronomical forcing during the past 35 million years. *Geology*, *45*(4), 375–378. https://doi.org/10.1130/G38663.1

Dettman, D. L., Kohn, M. J., Quade, J., Ryerson, F. J., Ojha, T. P., & Hamidullah, S. (2001). Seasonal stable isotope evidence for a strong Asian monsoon throughout the past 10.7 m.y. *Geology*, *29*(1), 31–34. https://doi.org/10.1130/0091-7613(2001)029<0031:SSIEFA>2.0.CO;2

Evans, D., & Müller, W. (2012). Deep time foraminifera Mg/Ca paleothermometry: Nonlinear correction for secular change in seawater mg/ca. *Paleoceanography*, *27*, PA4205. https://doi.org/10.1029/2012PA002315

Farnsworth, A., Lunt, D. J., Robinson, S. A., Valdes, P. J., Roberts, W. H. G., Clift, P. D., et al. (2019). Past East Asian monsoon evolution controlled by paleogeography, not CO_2. *Science Advances*, *5*(3). https://doi.org/10.1126/sciadv.aav2189

Fennig, K., Andersson, A., Bakan, S., Klepp, C., & Schroeder, M. (2012). Hamburg ocean atmosphere parameters and fluxes from satellite data—HOAPS 3.2—Monthly means/6-hourly composites. Satellite Application Facility on Climate Monitoring. https://doi.org/10.5676/EUM_SAF_CM/HOAPS/V001

Flores, J. A., Johnson, J. E., Mejía-Molina, A. E., Álvarez, M. C., Sierro, F. J., Singh, S. D., et al. (2014). Sedimentation rates from calcareous nannofossil and planktonic foraminifera biostratigraphy in the Andaman Sea, northern Bay of Bengal, and eastern Arabian Sea. *Marine and Petroleum Geology*, *58*, 425–437. https://doi.org/10.1016/j.marpetgeo.2014.08.011

Flower, B. P., & Kennett, J. P. (1994). The middle Miocene climatic transition: East Antarctic ice sheet development, deep ocean circulation and global carbon cycling. *Palaeogeography, Palaeoclimatology, Palaeoecology*, *108*(3–4), 537–555. https://doi.org/10.1016/0031-0182(94)90251-8

Fore, A. G., Yueh, S. H., Tang, W., Stiles, B. W., & Hayashi, A. K. (2016). Combined active/passive retrievals of ocean vector wind and sea surface salinity with SMAP. *IEEE Transactions on Geoscience and Remote Sensing*, *54*(12), 7396–7404. https://doi.org/10.1109/TGRS.2016.2601486

Frisch, K., Voigt, S., Verestek, V., Appel, E., Albert, R., Gerdes, A., et al. (2019). Long-period astronomical forcing of westerlies' strength in central Asia during Miocene climate cooling. *Paleoceanography and Paleoclimatology*, *34*, 1784–1806. https://doi.org/10.1029/2019PA003642

Gradstein, F. M., Ogg, J. G., & Smith, A. G. (2004). *A geologic time scale 2004* (p. 589). Cambridge: Cambridge University Press.

Groeneveld, J., Filipsson, H. L., Austin, W. E. N., Darling, K., McCarthy, D., Krupinski, N. B. Q., et al. (2018). Assessing proxy signatures of temperature, salinity, and hypoxia in the Baltic Sea through foraminifera-based geochemistry and faunal assemblages. *Journal of Micropalaeontology*, *37*(2), 403–429. https://doi.org/10.5194/jm-37-403-2018

Groeneveld, J., Henderiks, J., Renema, W., McHugh, C. M., De Vleeschouwer, D., Christensen, B. A., et al. (2017). Australian shelf sediments reveal shifts in Miocene Southern Hemisphere westerlies. *Science Advances*, *3*, e1602567. https://doi.org/10.1126/sciadv.1602567

Gunnell, Y., Gallagher, K., Carter, A., Widdowson, M., & Hurford, A. J. (2003). Denudation history of the continental margin of western peninsular India since the early Mesozoic-reconciling apatite fission-track data with geomorphology. *Earth and Planetary Science Letters*, *215*(1–2), 187–201. https://doi.org/10.1016/s0012-821x(03)00380-7

Gupta, A. K., Yuvaraja, A., Prakasam, M., Clemens, S. C., & Velu, A. (2015). Evolution of the South Asian monsoon wind system since the late Middle Miocene. *Palaeogeography, Palaeoclimatology, Palaeoecology*, *438*, 160–167. https://doi.org/10.1016/j.palaeo.2015.08.006

Hamon, N., Sepulchre, P., Lefebvre, V., & Ramstein, G. (2013). The role of eastern Tethys seaway closure in the Middle Miocene Climatic Transition (ca. 14 Ma). *Climate of the Past*, *9*(6), 2687–2702. https://doi.org/10.5194/cp-9-2687-2013

Hasiuk, F. J., & Lohmann, K. C. (2010). Application of calcite Mg partitioning functions to the reconstruction of paleocean Mg/Ca. *Geochimica et Cosmochimica Acta*, *74*(23), 6751–6763. https://doi.org/10.1016/j.gca.2010.07.030

Herold, N., Huber, M., & Mueller, R. D. (2011). Modeling the Miocene Climatic Optimum. Part I: Land and atmosphere. *Journal of Climate*, *24*(24), 6353–6372. https://doi.org/10.1175/2011JCLI4035.1

Holbourn, A., Kuhnt, W., Clemens, S., Prell, W., & Andersen, N. (2013). Middle to late Miocene stepwise climate cooling: Evidence from a high-resolution deep water isotope curve spanning 8 million years. *Paleoceanography*, *28*, 688–699. https://doi.org/10.1002/2013PA002538

Holbourn, A., Kuhnt, W., Regenberg, M., Schulz, M., Mix, A., & Andersen, N. (2010). Does Antarctic glaciation force migration of the tropical rain belt? *Geology*, *38*(9), 783–786. https://doi.org/10.1130/g31043.1

Holbourn, A. E., & Henderson, A. S. (2002). Re-illustration and revised taxonomy for selected deep-sea benthic foraminifers. *Palaeontologia Electronica*, *4*(2), 1–34. http://palaeoelectronica.org/paleo/2001_2/foram/issue2_01.htm

Holbourn, A. E., Kuhnt, W., Clemens, S. C., Kochhann, K. G. D., Johnck, J., Lubbers, J., & Andersen, N. (2018). Late Miocene climate cooling and intensification of southeast Asian winter monsoon. *Nature Communications*, *9*, 1584. https://doi.org/10.1038/s41467-018-03950-1

Holbourn, A. E., Kuhnt, W., Schulz, M., & Erlenkeuser, H. (1995). Impacts of orbital forcing and atmospheric carbon dioxide on Miocene ice-sheet expansion. *Nature*, *438*, 483–487.

Holbourn, A. E., Kuhnt, W., Schulz, M., Flores, J.-A., & Andersen, N. (2007). Middle Miocene long-term climate evolution: Eccentricity modulation of the "Monterey" carbon-isotope excursion. *Earth and Planetary Science Letters*, *261*(3–4), 534–550. https://doi.org/10.1016/j.epsl.2007.07.026

Hönisch, B., Allen, K. A., Russell, A. D., Eggins, S. M., Bijma, J., Spero, H. J., et al. (2011). Planktic foraminifers as recorders of sea water Ba/Ca. *Marine Micropaleontology*, *79*(1–2), 52–57. https://doi.org/10.1016/j.marmicro.2011.01.003

Hoorn, C., Ohja, T., & Quade, J. (2000). Palynological evidence for vegetation development and climatic change in the sub-Himalayan zone (Neogene, Central Nepal). *Palaeogeography, Palaeoclimatology, Palaeoecology*, *163*(3–4), 133–161. https://doi.org/10.1016/S0031-0182(00)00149-8

Horita, J., Zimmermann, H., & Holland, H. D. (2002). Chemical evolution of seawater during the Phanerozoic: Implications from the record of marine evaporites. *Geochimica et Cosmochimica Acta*, *66*(21), 3733–3756. https://doi.org/10.1016/S0016-7037(01)00884-5

Hormann, V., Centurioni, L. R., & Gordon, A. L. (2019). Freshwater export pathways from the Bay of Bengal. *Deep-Sea Research Part II*, *168*, 104645. https://doi.org/10.1016/j.dsr2.2019.104645

Huang, Y., Clemens, S. C., Liu, W., Wang, Y., & Prell, W. L. (2007). Large-scale hydrological change drove the late Miocene C4 plant expansion in the Himalayan foreland and Arabian Peninsula. *Geology*, *35*(6), 531. https://doi.org/10.1130/G23666A.1

Huber, M., & Goldner, A. (2012). Eocene monsoons. *Journal of Asian Earth Sciences*, *44*, 3–23. https://doi.org/10.1016/j.jseaes.2011.09.014

Kiefer, T., McCave, I. N., & Elderfield, H. (2006). Antarctic control on tropical Indian Ocean sea surface temperature and hydrography. *Geophysical Research Letters*, *33*, L24612. https://doi.org/10.1029/2006GL027097

Kroon, D., Steens, T., & Troelstra, S. R. (1991). Onset of monsoonal related upwelling in the western Arabian Sea as revealed by planktonic foraminifers. In W. L. Prell, N. Niitsuma, et al. (Eds.), *Proceedings of the Ocean Drilling Program, Scientific Results* (Vol. 117, pp. 257–263). College Station, Texas: Ocean Drilling Program.

Laskar, J., Robutel, P., Joutel, F., Gastineau, M., Correia, A., & Levrard, B. (2004). A long-term numerical solution for the insolation quantities of the Earth. *Astronomy & Astrophysics*, *428*(1), 261–285. https://doi.org/10.1051/0004-6361:20041335

Lea, D. W., & Boyle, E. A. (1991). Barium in planktonic foraminifera. *Geochimica et Cosmochimica Acta*, *55*(11), 3321–3331. https://doi.org/10.1016/0016-7037(91)90491-m

Licht, A., van Cappelle, M., Abels, H. A., Ladant, J.-B., Trabucho-Alexandre, J., France-Lanord, C., et al. (2014). Asian monsoons in a late Eocene greenhouse world. *Nature*, *513*, 501–506. https://doi.org/10.1038/nature13704

Liu, Z., & Yang, H. (2003). Extratropical control of tropical climate, the atmospheric bridge and oceanic tunnel. *Geophysical Research Letters*, *30*(5), 1230. https://doi.org/10.1029/2002GL016492

Liu, X., & Yin, Z.-Y. (2002). Sensitivity of East Asian monsoon climate to the uplift of the Tibetan Plateau. *Palaeogeography, Palaeoclimatology, Palaeoecology*, *183*, 223–245.

Martinez-Mendez, G., Hebbeln, D., Mohtadi, M., Lamy, F., De Pol-Holz, R., Reyes-Macaya, D., & Freudenthal, T. (2013). Changes in the advection of Antarctic Intermediate Water to the northern Chilean coast during the last 970 kyr. *Paleoceanography*, *28*, 607–618. https://doi.org/10.1002/palo.20047

Milliman, J. D., & Farnsworth, K. L. (2011). *River discharge to the coastal ocean: A global synthesis* (p. 392). Cambridge: Cambridge University Press. https://doi.org/10.1017/CBO9780511781247

Mohtadi, M., Lückge, A., Steinke, S., Groeneveld, J., Hebbeln, D., & Westphal, N. (2010). Late Pleistocene surface and thermocline conditions of the eastern tropical Indian Ocean. *Quaternary Science Reviews*, *29*, 887–896. https://doi.org/10.1016/j.quascirev.2009.12.006

Mohtadi, M., Prange, M., Oppo, D. W., De Pol-Holz, R., Merkel, U., Zhang, X., et al. (2014). North Atlantic forcing of tropical Indian Ocean climate. *Nature*, *509*(7498), 76–80. https://doi.org/10.1038/nature13196

Muggeo, V. M. R. (2003). Estimating regression models with unknown break-points. *Statistics in Medicine*, *22*(19), 3055–3071. https://doi.org/10.1002/sim.1545

Muggeo, V. M. R. (2008). Segmented: An R package to fit regression models with broken-line relationships. *R News*, *8*(1), 20–25. https://cran.r-project.org/doc/Rnews/

Nigrini, C. (1991). Composition and biostratigraphy of radiolarian assemblages from an area of upwelling (Northwestern Arabian Sea, Leg 117). In *Proceeding of the Ocean Drilling Program*, *Scientific Results* (Vol. 117, pp. 89–126). College Station, TX: Ocean Drilling Program. https://doi.org/10.2973/odp.proc.sr.117.132.1991

Nürnberg, D. (2000). Paleoclimate: Taking the temperature of past ocean surfaces. *Science*, *289*(5485), 1698–1699. https://doi.org/10.1126/science.289.5485.1698

Ouimet, W., Whipple, K., Royden, L., Reiners, P., Hodges, K., & Pringle, M. (2010). Regional incision of the eastern margin of the Tibetan Plateau. *Lithosphere*, *2*(1), 50–63. https://doi.org/10.1130/L57.1

Paillard, D., Labeyrie, L., & Yiou, P. (1996). Macintosh program performs time-series analysis. *Eos, Transactions American Geophysical Union*, *77*(39), 379–379. https://doi.org/10.1029/96EO00259

Pena, L., Goldstein, S., Hemming, S., Jones, K., Calvo, E., Pelejero, C., & Cacho, I. (2013). Rapid changes in meridional advection of Southern Ocean intermediate waters to the tropical Pacific during the last 30 kyr. *Earth and Planetary Science Letters*, *368*, 20–32. https://doi.org/10.1016/j.epsl.2013.02.028

Pena, L. D., Calvo, E., Cacho, I., Eggins, S., & Pelejero, C. (2005). Identification and removal of Mn-Mg-rich contaminant phases on foraminiferal tests: Implications for Mg/Ca past temperature reconstructions. *Geochemistry, Geophysics, Geosystems*, *6*, Q09P02. https://doi.org/10.1029/2005GC000930

Prasad, M. (1993). Siwalik (middleMiocene)woods from the Kalagarh area in theHimalayan foot hills and their bearing on paleoclimate and phytogeography. *Review of Palaeobotany and Palynology*, *76*(1), 49–82. https://doi.org/10.1016/0034-6667(93)90080-E

Prasad, T. G., Ikeda, M., & Prasanna Kumar, S. (2001). Seasonal spreading of the Persian Gulf Water mass in the Arabian Sea. *Journal of Geophysical Research*, *106*(C8), 17,059–17,071. https://doi.org/10.1029/2000JC000480

Prasanna Kumar, S., Narvekar, J., Kumar, A., Shaji, C., Anand, P., Sabu, P., et al. (2004). Intrusion of the Bay of Bengal water into the Arabian Sea during winter monsoon and associated chemical and biological response. *Geophysical Research Letters*, *31*, L15304. https://doi.org/10.1029/2004GL020247

Reuter, M., Kern, A. K., Harzhauser, M., Kroh, A., & Piller, W. E. (2013). Global warming and South Indian monsoon rainfall-lessons from the Mid-Miocene. *Gondwana Research*, *23*(3), 1172–1177. https://doi.org/10.1016/j.gr.2012.07.015

Romahn, S., Mackensen, A., Groeneveld, J., & Pätzold, J. (2014). Deglacial intermediate water reorganization: New evidence from the Indian Ocean. *Climate of the Past*, *10*, 293–303. https://doi.org/10.5194/cp-10-293-2014

Saraswat, R., Lea, D. W., Nigam, R., Mackensen, A., & Naik, D. K. (2013). Deglaciation in the tropical Indian Ocean driven by interplay between the regional monsoon and global teleconnections. *Earth and Planetary Science Letters*, *375*, 166–175. https://doi.org/10.1016/j.epsl.2013.05.022

Sarkar, A., Ramesh, R., Somayajulu, B. L. K., Agnihotri, R., Jull, A. J. T., & Burr, G. S. (2000). High resolution Holocene monsoon record from the eastern Arabian Sea. *Earth and Planetary Science Letters*, *177*(3–4), 209–218. https://doi.org/10.1016/s0012-821x(00)00053-4

Schiemann, R., Lüthis, D., & Schär, C. (2009). Seasonality and interannual variability of the westerly jet in the Tibetan Plateau region. *Journal of Climate*, *22*(11), 2940–2957. https://doi.org/10.1175/2008JCLI2625.1

Schott, F. A., & McCreary, J. P. (2001). The monsoon circulation of the Indian Ocean. *Progress in Oceanography*, *51*(1), 1–123. https://doi.org/10.1016/S0079-6611(01)00083-0

Scotese, C. R. (2002). PALEOMAP website. http://www.scotese.com

Sexton, P. F., Wilson, P. A., & Pearson, P. N. (2006). Microstructural and geochemical perspectives on planktic foraminiferal preservation: "Glassy" versus "Frosty". *Geochemistry, Geophysics, Geosystems*, *7*, Q12P19. https://doi.org/10.1029/2006GC001291

Shackleton, N. J., & Opdyke, N. D. (1973). Oxygen isotope and palaeomagnetic stratigraphy of Equatorial Pacific core V28-238: Oxygen isotope temperatures and ice volumes on a 10^5 year and 10^6 year scale. *Quaternary Research*, *3*(1), 39–55. https://doi.org/10.1016/0033-5894(73)90052-5

Shevenell, A. E., Kennett, J. P., & Lea, D. W. (2004). Middle Miocene Southern Ocean cooling and Antarctic cryosphere expansion. *Science*, *305*(5691), 1766–1770. https://doi.org/10.1126/science.1100061

Shevenell, A. E., Kennett, J. P., & Lea, D. W. (2008). Middle Miocene ice sheet dynamics, deep-sea temperatures, and carbon cycling: A Southern Ocean perspective. *Geochemistry, Geophysics, Geosystems*, *9*, Q02006. https://doi.org/10.1029/2007GC001736

Sosdian, S. M., Babila, T. L., Greenop, R., Foster, G. L., & Lear, C. H. (2020). Ocean Carbon Storage across the middle Miocene: A new interpretation for the Monterey Event. *Nature Communications*, *11*, 134. https://doi.org/10.1038/s41467-019-13792-0

Srivastava, G., Paudayal, N., Utescher, T., & Mehrotra, R. C. (2018). Miocene vegetation shift and climate change: Evidence from the Siwalik of Nepal. *Global and Planetary Change*, *161*, 108–120. https://doi.org/10.1016/j.gloplacha.2017.12.001

Stanley, S. M., & Hardie, L. A. (1998). Secular oscillations in the carbonate mineralogy of reef-building and sediment-producing organisms driven by tectonically forced shifts in seawater chemistry. *Palaeogeography, Palaeoclimatology, Palaeoecology*, *144*(1–2), 3–19. https://doi.org/10.1016/s0031-0182(98)00109-6

Steinke, S., Groeneveld, J., Johnstone, H., & Rendle-Bühring, R. (2010). East Asian summer monsoon weakening after 7.5 Ma: Evidence from combined planktonic foraminifera Mg/Ca and $\delta^{18}O$ (ODP Site 1146; northern South China Sea). *Palaeogeography, Palaeoclimatology Palaeoecology*, *289*(1–4), 33–43. https://doi.org/10.1016/j.palaeo.2010.02.007

Thunell, R. C. (1976). Optimum indices of calcium carbonate dissolution in deep-sea sediments. *Geology*, *4*(9), 525–527. https://doi.org/10.1130/0091-7613(1976)4<525:OIOCCD>2.0.CO;2

You, Y. (1998). Intermediate water circulation and ventilation of the Indian Ocean derived from water-mass contributions. *Journal of Marine Research*, *56*, 1029–1067.

Yu, J., Day, J., Greaves, M., & Elderfield, H. (2005). Determination of multiple element/calcium ratios in foraminiferal calcite by quadrupole ICP-MS. *Geochemistry, Geophysics, Geosystems*, *6*, Q08P01. https://doi.org/10.1029/2005GC000964

Zachos, J. C., Dickens, G. R., & Zeebe, R. E. (2008). An early Cenozoic perspective on greenhouse warming and carbon-cycle dynamics. *Nature*, *451*(7176), 279–283. https://doi.org/10.1038/nature06588

Zhang, R., Jiang, D., Zhang, Z., & Yu, E. (2015). The impact of regional uplift of the Tibetan Plateau on the Asian monsoon climate. *Palaeogeography, Palaeoclimatology, Palaeoecology*, *417*, 137–150. https://doi.org/10.1016/j.palaeo.2014.10.030

Zhang, Y. G., Pagani, M., Liu, Z., Bohaty, S. M., & DeConto, R. (2013). A 40-million-year history of atmospheric CO_2. *Philosophical Transactions of the Royal Society A: Mathematical, Physical and Engineering Sciences*, *371*. https://doi.org/10.1098/rsta.2013.0096

Zhuang, G., Pagani, M., & Zhang, Y. G. (2017). Monsoonal upwelling in the western Arabian Sea since the middle Miocene. *Geology*, *45*(7), 655–658. https://doi.org/10.1130/G39013.1